Unsupervised Stain Decomposition via Inversion Regulation for Multiplex Immunohistochemistry Images

Author name(s) withheld EMAIL(S) WITHHELD
Address withheld

Editors: Under Review for MIDL 2023

Abstract

Multiplex Immunohistochemistry (mIHC) is a cost-effective and accessible method for in situ labeling of multiple protein biomarkers in a tissue sample. By assigning a different stain to each biomarker, it allows the visualization of different types of cells within the tumor vicinity for downstream analysis. However, to detect different types of stains in a given mIHC image is a challenging problem, especially when the number of stains is high. Previous deep-learning-based methods mostly assume full supervision; yet the annotation can be costly. In this paper, we propose a novel unsupervised stain decomposition method to detect different stains simultaneously. Our method does not require any supervision, except for color samples of different stains. A main technical challenge is that the problem is underdetermined and can have multiple solutions. To conquer this issue, we propose a novel inversion regulation technique, which eliminates most undesirable solutions. On a 7-plexed IHC image dataset, the proposed method achieves high quality stain decomposition results without human annotation.

Keywords: Color deconvolution, Deep learning, Multiplex, Immunohistochemistry, Unsupervised.

1. Introduction

Multiplex Immunohistochemistry (mIHC) is a tissue imaging technique that allows simultaneous detection of multiple biomarkers in the same tissue section. Multiplex imaging has become an important tool in diagnostic pathology and cancer immunotherapy. It enables the study of cell composition, cellular function and cell-cell interactions, not to mention, allowing a more in depth comprehension and profiling of the tumor micorenvironment (Ilié et al., 2018; Johnson et al., 2018; Remark et al., 2016; Tan et al., 2020). While there are various multiplex imaging technologies, mIHC is a cost effective and accessible method that can be captured in a single step with traditional brightfield light microscopy. Moreover, it does not require any special software or visualization tools, making biomarker research and profiling more accessible (Tan et al., 2020). mIHC offers simultaneous staining of 5+ biomarkers (Tan et al., 2020; Fassler et al., 2020; Hofman et al., 2019; Dixon et al., 2015). Unlike more expensive multiplex imaging techniques, e.g., multiplex immunofluorescence, mIHC does not offer separate channels for different biomarkers. It rather provides a single image with all the biomarkers visualized together, see Figure 1 (left). The simultaneous staining in mIHC images can offer insights into the tumor microenvironment that are not obtainable with singly stained IHC images but it still requires much manual effort to analyze. Visual inspection is both challenging and time consuming for pathologists, especially with increasing number of stains.

© 2023 Anonymous.

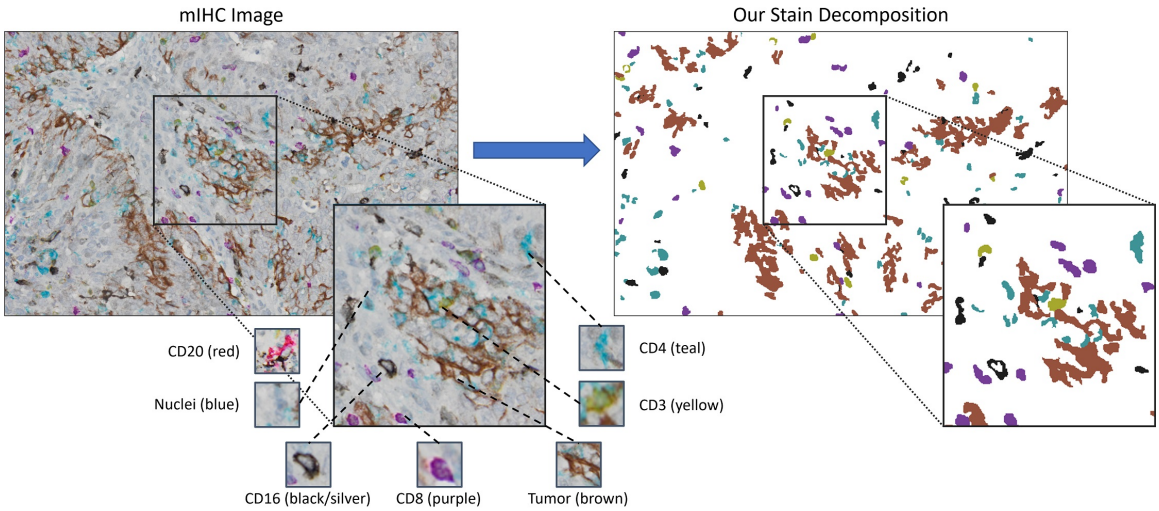

Figure 1: An mIHC image and the corresponding unsupervised stain decomposition. Samples from the different biomarkers are shown. The CD20 sample is from a different image since it is not present in this view. The yellow staining looks like olive yellow because of the interaction with the blue nuclei staining.

To analyze the images at a large scale, this process needs to be automated. The images need to be decomposed into individual biomarker maps before any spatial analysis or quantification can take place (Compare the left- and right-hand sides in Figure 1). To that end, digital analysis methods are essential to automate the stain unmixing, i.e., extracting masks corresponding to different biomarkers (Van Herck et al., 2021) to use them for tumor microenvironment analysis (Fassler et al., 2020).

Color deconvolution is the unmixing of stains into separate stain concentration maps. Several unsupervised color deconvolution methods (Ruifrok and Johnston, 2001; Vahadane et al., 2016; Macenko et al., 2009) have been successfully deployed for the analysis of up to two biomarkers, such as hematoxylin and eosin (H&E). Extending to a larger number of stains involves solving an under-determined linear equation system, which can have many undesired solutions. To address this issue, in (Chen and Chefd'hotel, 2014; Chen and Srinivas, 2015), a lasso regression model is proposed to select a sparse set of stains at each pixel. The results, however, are not satisfying, mostly because these methods treat different pixels independently, and fail to consider the contextual information. In (Duggal et al., 2017) dual-stained images are implicitly deconvolved for downstream classification tasks, but the deconvolution channels are not guaranteed to accurately correspond to the different stains. Commercial tools such as HALO can unmix up to 4-colored chromogenic stains (Thommen et al., 2018). More recently, (Abousamra et al., 2020) proposed a weakly supervised deep learning approach for stain decomposition. Its performance depends on manual annotations of cell centers, which can be very time consuming.

In this work, we propose an unsupervised mIHC stain decomposition method that can scale to a larger number of stains. Our method only requires the reference stain colors. To

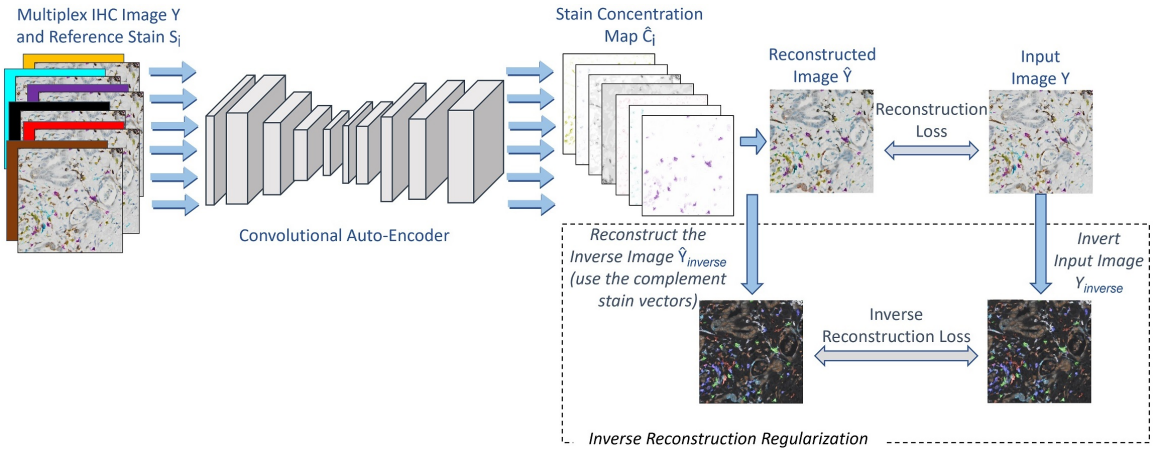

Figure 2: Proposed model architecture and training. The model's output is conditioned on the input mIHC image and the target reference stain. It is trained with a reconstruction loss and an inverse reconstruction loss.

properly leverage contextual information, we use a convolutional neural network autoencoder to generate the stain concentration maps. With an increased number of stains, the solution is not unique. Using the sparsity prior is not the best solution as it fails to consider the context. To this end, we propose a novel inverse-image-based regularization loss to help the network learn high quality stain concentration maps. We show how different cell types or biomarker segmentation maps can be directly inferred from the resulting concentration maps. On a 7-plex mIHC images dataset, we show the effectiveness of our proposed approach, achieving evaluation scores very close to the supervised method (Abousamra et al., 2020) ($\sim 94\%$ of the supervised f-score on average).

2. Related Work

Stain unmixing/decomposition is a classical problem that has been studied extensively on histological images, e.g., H&E. Ruifrok and Johnston (2001) were the first to use the optical density color representation to address the problem. The decomposition problem is transformed into solving a linear equation system. Different decomposition methods have been proposed (Macenko et al., 2009; Alsubaie et al., 2016, 2017; Vahadane et al., 2016; Hidalgo-Gavira et al., 2018; Pérez-Bueno et al., 2020).

Recent years have witnessed rapid advancement of staining technology; one may acquire simultaneous staining of more than 2 biomarkers in the same tissue section. See example in Figure 1. However, with mIHC allowing 9+ simultaneous stains (Tan et al., 2020), stain unmixing becomes more challenging and new methods are needed to handle a large number of stains. Chen and Chefd'hotel (2014) extended the work of (Ruifrok and Johnston, 2001) to support more than 2 stains. With more than 3 stains, the optical-density-based linear equation system is underdetermined. To address the issue, lasso regression was proposed. Nevertheless, directly enforcing a sparsity prior is not sufficient especially for higher number

of stains, mainly because the sparsity prior fails to consider contextual information of each pixel. (Chen and Srinivas, 2015) further adds constraints on the lasso regression to model co-staining. Abousamra et al. (2020) proposes to use weak supervision in the form of dot annotations that are transformed into superpixels (Achanta et al., 2012) to overcome the underdetermined nature of the problem. They train a convolutional autoencoder to estimate the concentration maps and show the effectiveness of the method in decomposing 6 simultaneous stained mIHC images. Their method, however, still requires a large amount of annotations, which can be prohibitive in practice. For completeness, we also refer to methods that directly incorporate color deconvolution into downstream tasks (Duggal et al., 2017; Lahiani et al., 2018), e.g., tissue segmentation.

3. Background

MIHC images are obtained by histologic detection of multiple protein biomarkers. In this section we describe the linear relationship of stain concentrations under Beer Lambert law. This is the basis for most stain unmixing methods including ours.

Optical Density (OD). Optical density measures the absorption of light as it passes through a medium. The optical density at a pixel i is the negative log of its normalized RGB values, $[r_i, g_i, b_i]^T \in [0,1]^3$:

$$\boldsymbol{y}_i = [-\log(r_i), -\log(g_i), -\log(b_i)]^T. \tag{1}$$

The stains and their concentrations are linearly related in the OD space. Assume a given set of m stain vectors, whose OD vectors are represented by the matrix $\boldsymbol{S} = [\boldsymbol{s}_1, \boldsymbol{s}_2, \cdots, \boldsymbol{s}_m] \in \mathbb{R}^{3\times m}$, where $\boldsymbol{s}_j \in \mathbb{R}^3$ is the OD vector of the jth stain. By Beer Lambert Law (BL) (Lambert, 1760), for any pixel i, the optical density $\boldsymbol{y}_i$ and its stain concentration vector $\boldsymbol{c}_i$ satisfy a linear relationship, i.e., $\boldsymbol{y}_i = \boldsymbol{S} \cdot \boldsymbol{c}_i$, where $\boldsymbol{c}_i \in \mathbb{R}^m$ denotes the concentrations of the different stains at pixel i. Generalizing to an image with n pixels, we get:

$$\boldsymbol{Y} = [\boldsymbol{y}_1, \cdots, \boldsymbol{y}_n] = \boldsymbol{S} \cdot \boldsymbol{C} \tag{2}$$

in which $\boldsymbol{Y} \in \mathbb{R}^{3\times n}$ is the optical density matrix of all the pixels in the image and $\boldsymbol{C} = [\boldsymbol{c}_1, \cdots, \boldsymbol{c}_n] \in \mathbb{R}^{m\times n}$ is the corresponding stains' concentrations matrix.

Solving the Linear Equation. The stain mixing was first modeled by (Ruifrok and Johnston, 2001) using Beer Lambert Law. Given the reference stains matrix $\boldsymbol{S}$, they proposed to recover the stain concentrations by solving the linear equation system, Equation (2). In practice, stain color vectors are obtained by sampling representative pixels of each stain. A background color vector is often added as an additional stain. However, for higher than 2-plex staining i.e., when the stain matrix S consists of more than 3 stain vectors (2 biomarker stains and the background), the linear equation system is underdetermined and does not have a unique solution.

4. Method: InverseAE for Unsupervised Stain Decomposition

In this work we propose *InverseAE*, an unsupervised deep-learning stain decomposition method. Our proposed method results in meaningful stain concentration maps from which

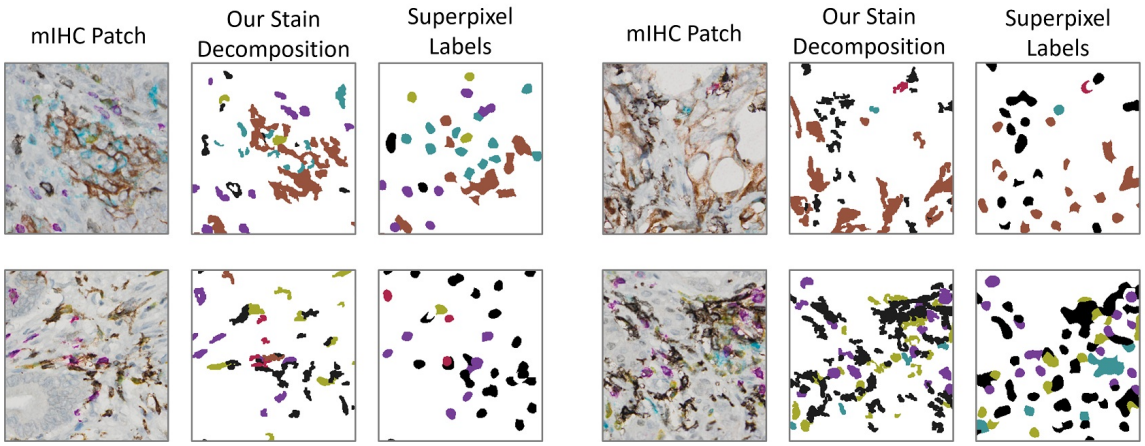

Figure 3: Sample mIHC patches, our corresponding unsupervised stain decomposition, and the superpixel labels derived from the dot annotations.

Table 1: F-score of stain segmentations with respect to dot annotations on 96 patches from 42 cases.

Method	CD3	CD4	CD8	CD16	CD20	Tumor	Mean
PseudoInv	0.158	0.208	0.441	0.267	0.265	0.403	0.290
Nearest Neighbor	0.223	0.168	0.734	0.277	0.106	0.357	0.311
LassoReg	0.456	0.501	0.801	0.050	0.223	0.389	0.404
UNet (supervised)	0.496	0.496	**0.835**	0.699	0.144	0.405	0.513
ColorAE (supervised)	0.639	**0.585**	0.829	**0.728**	**0.353**	**0.573**	**0.618**
InverseAE	**0.644**	0.530	0.813	0.632	0.327	0.556	0.584

the dominant stain/biomarker at each pixel can be inferred directly. It only requires the set of multiplex stained images and the set of reference stains color vectors.

We use a conditional autoencoder to generate the stain concentration maps for an input image. The input to the model is the mIHC image $\boldsymbol{Y}$ and a single target reference stain $\boldsymbol{S}_i$, and the output is the concentration map for that stain $\widehat{\boldsymbol{C}_i}$. This formulation of the output conditioned on the input stain is to reduce overfitting. The target stain is input to the model as a normalized image where all the pixels take the value of the reference stain vector and is appended to the mIHC image as additional channels. After collecting all the stain concentration maps $\widehat{\boldsymbol{C}}$, Beer Lambert's law is then used to reconstruct the image $\widehat{\boldsymbol{Y}}$ See Figure 2

4.1. Training with Inverse Regulation

An autoencoder is generally trained with a reconstruction loss. Here we have $\mathcal{L}_{recon} = MSE(\boldsymbol{Y}, \boldsymbol{S} \cdot \widehat{\boldsymbol{C}})$ is aimed to solve Equation (2). It compares the image $\boldsymbol{Y}$ with the reconstructed image $\boldsymbol{S} \cdot \widehat{\boldsymbol{C}}$ using mean squared error. When the number of stain vectors $m > 3$,

Equation (2) becomes an underdetermined system of equations with possibly infinite number of solutions. We need to impose constraints that guide the network towards the *desired solution*, i.e., at each pixel the dominant stain gets the highest concentration value relative to the other stains.

To achieve this, we propose a novel *inverse reconstruction regularizer*. The key idea is to use the same estimated concentration maps to reconstruct the inverted image. We first define the *inverted optical density*. For an arbitrary pixel with normalized RGB color vector $[r,\ g,\ b]^T$, its *inverted optical density* is $\boldsymbol{y}_{inverse} = [-\log(1-r), -\log(1-g), -\log(1-b)]^T$. Similarly, $\boldsymbol{S}_{inverse}$ is the inverted optical density for the stain matrix $\boldsymbol{S}$. To regularize the solution of Equation (2), we add the inverted equations into the system.

$$\boldsymbol{y}_{inverse} = \boldsymbol{S}_{inverse} \cdot \boldsymbol{c}, \tag{3}$$

Hence the inverse reconstruction regularization loss is defined as:

$$\mathcal{L}_{inverse} = MSE(\boldsymbol{Y}_{inverse}, \boldsymbol{S}_{inverse} \cdot \widehat{\boldsymbol{C}}). \tag{4}$$

Using the inverse reconstruction loss, we observe that it pushes the prediction towards the desired solution; that is, at any location, the stain corresponding to the observed color gets the highest concentration. The overall loss function becomes:

$$\mathcal{L}_{unsup} = \lambda_1 \mathcal{L}_{recon} + \lambda_2 \mathcal{L}_{inverse} \tag{5}$$

where λ_1 and λ_2 are constant weight values, which are set to 1 in our experiments.

Next, we explain: (1) how the reconstruction permits the desired solution; and (2) why reconstructing the inverted image helps. First, the following lemma shows that reconstructing the inverted image permits the same set of one-hot concentration map.

Lemma 1 *Assuming all stains are different, a one-hot solution* $\boldsymbol{c}$ *satisfies the BL equation Equation (2) if and only if it satisfies the inverted BL equation Equation (3).*

Proof The inversion regulation is basically training the model to generate concentration maps that not only satisfy Equation (2) for a mIHC image Y and a set of stains S, but also satisfy it for the complement (or inverse) image $Y_{inverse}$ and the complement (or inverse) stains $S_{inverse}$. While there may be infinite solutions to Equation (2), we define a good solution as one where we can easily use to infer the stain segmentation map. For example, a sparse solution where at each location only the visually present biomarker s_i has a stain concentration $c_i > 0$ and the rest of the biomarkers have stain concentrations $c_j = 0 : j \in \{1, .., n\}, j \neq i$. Such a solution is ideal for inferring the stain segmentation map. We show that such a solution is supported by the use of the inversion regulation. By applying Equation (2) on the red component:

$$\log r = c_1 \log r_1 + \cdots + c_n \log r_n \tag{6}$$

and re-arranging

$$r = r_1^{c_1} \times \cdots \times r_n^{c_n} \tag{7}$$

Similarly, for the same pixel in the inverted image and stains and assuming the same set of stain concentrations:

$$\log(1-r) = c_1 \log(1-r_1) + \cdots + c_n \log(1-r_n) \tag{8}$$

$$1 - r = (1 - r_1)^{c_1} \times \cdots \times (1 - r_n)^{c_n} \tag{9}$$

From Equations 7 and 9:

$$1 - (r_1^{c_1} \dots r_n^{c_n}) = (1 - r_1)^{c_1} \dots (1 - r_n)^{c_n} \tag{10}$$

The same can be performed for the green and blue components:

$$1 - (g_1^{c_1} \dots g_n^{c_n}) = (1 - g_1)^{c_1} \dots (1 - g_n)^{c_n} \tag{11}$$

$$1 - (b_1^{c_1} \dots b_n^{c_n}) = (1 - b_1)^{c_1} \dots (1 - b_n)^{c_n} \tag{12}$$

From Equations 10-12, if a one hot solution exists for an image and set of stains, it will also satisfies the inverted image and inverted stains. ■

Therefore, by adding the inversion regulation, we add more constraints to the solution space. It is more likely we will derive a desirable one-hot solution.

Second, we would like to point out that the choice of inverted image is not a coincidence. When an object absorbs light of a particular color, we perceive the object as having the complementary color. This special relationship between a color and its complementary (or inverse) inspires our idea of reconstructing the inverted image. In the HSL color space, a color and its inverse share the same saturation value, see Section C. The saturation measures the departure of a hue from white (Agoston, 2005) and thus correlates with the amount of pigment present, i.e. its concentration. As a result, a color and its inverse share physical properties, such that there exists a solution concentration matrix that satisfies Beer Lambert Law for an image and a set of stain vectors as well as for the inverted version of the image and the stain vectors.

4.2. Stain Segmentation Maps Inference.

The ultimate goal is to get a semantic segmentation map of the stains. Such a map would reflect the presence of different biomarkers or cell types to utilize in downstream analysis. The resulting concentration from our unsupervised solution can be used directly to do just that without further annotation or training. Each stain has a minimum concentration value below which the stain can be excluded from the competition for the dominating stain. During inference, each stain concentration map is thresholded and then an argmax function is applied to select the stain with the maximal concentration at each location. The resulting segmentation map has a single stain prediction at each pixel, reflecting the predicted dominant stain at each location. The threshold parameters are fixed for each stain and are empirically selected on a small held out set. See sample results in Figure 3.

5. Experiments

We performed experiments with 7-plex mIHC stained pancreatic cancer tissue. The 7 biomarkers include immune cell biomarkers: CD3 (yellow), CD4 (teal), CD8 (purple), CD16 (black), CD20 (red), and a tumor biomarker (brown), in addition to hematoxylin as a nuclear counterstain (blue). The training dataset consisted of 240 patches of size 400 $\times$ 400 at $20x$ divided into training and validation. See Section A for more details. Next, we

Table 2: Evaluation of Concentration Maps Using Structure Similarity Score on Single Stain Images.

Method	CD3	CD4	CD8	CD16	CD20	Tumor	Mean
ColorAE	0.893	**0.886**	**0.897**	0.657	0.876	**0.834**	0.841
InverseAE	**0.935**	0.881	0.879	**0.682**	**0.881**	0.800	**0.843**

present experiments for evaluating the predicted stain segmentation maps and for evaluating the quality of the raw concentration maps. An ablation study of the effect of different components on the model is in Section B

Evaluation with Dot Annotations. We tested the model on 96 patches of size 1200×1920 from 42 cases. These test patches have manual dot annotations for each biomarker where each dot marks the approximate center of a cell. The dot annotations are expanded to superpixels (Achanta et al., 2012) for visualization in second row of Figure 3. We compute the F-score for the predicted semantic segmentation maps for each biomarker, based on whether or not the generated segments intersect with the dot annotations of the corresponding biomarker. Details of F-score computation are in Section A. Table 1 shows the F-score results. We compare our method *InverseAE* to the supervised models *ColorAE* and *UNet* (Ronneberger et al., 2015), and to the unsupervised methods *LassoReg* (Chen and Chefd'hotel, 2014), *PseudoInv* which is an extension of (Ruifrok and Johnston, 2001) to support a stain matrix with > 3 stains using matrix pseudo inverse, and *Nearest Neighbor* which basically assigns the stain with the closest Euclidean distance to the pixel color value. See Section A for a description of the baselines. From Table 1, *InverseAE* outperforms all other unsupervised methods, coming at close second after *ColorAE*. Figure 3 shows sample results from *InverseAE*.

Evaluation with Ground Truth Concentration Maps. We assessed the quality of the concentration maps of the trained *InverseAE* and *ColorAE* models compared to 2-plex SOTA stain decomposition method (Vahadane et al., 2016) on a set of IHC 2-plex images using structure similarity index (SSIM). The 2-plex images were stained with one of the immune/tumor biomarkers plus hematoxylin. The results are in Table 2. Interestingly, the SSIM scores for *InverseAE* are often better than those for *ColorAE* showing that it better captures the continuous values of the concentration maps.

6. Conclusion

With the continuous increase in the number of simultaneous staining in multiplex IHC images and its technological and economical accessibility to a larger community, it is important to automate the analysis of the resulting multiplex-stained images. In this work, we have tackled the problem of stain decomposition in multiplex IHC images with relatively large number of stains. We propose unsupervised that can relieve pathologists from the burden of annotation to get accurate results. Our proposed method can be directly used to obtain stain semantic segmentation maps. We show that our proposed method *InverseAE* trained with additional constraints allow the model to learn to capture the correct cell types and the resulting stain concentration maps are representative of the underlying staining.

References

S. Abousamra, D. Fassler, L. Hou, Y. Zhang, R. Gupta, T. Kurc, L. F. Escobar-Hoyos, D. Samaras, B. Knudson, K. Shroyer, J. Saltz, and C. Chen. Weakly-supervised deep stain decomposition for multiplex ihc images. In *IEEE 17th International Symposium on Biomedical Imaging (ISBI)*, pages 481–485, 2020. doi: 10.1109/ISBI45749.2020.9098652.

R. Achanta, A. Shaji, K. Smith, A. Lucchi, P. Fua, and S. Süsstrunk. Slic superpixels compared to state-of-the-art superpixel methods. *IEEE Transactions on Pattern Analysis and Machine Intelligence*, 34(11):2274–2282, Nov 2012. ISSN 0162-8828. doi: 10.1109/TPAMI.2012.120.

M.K. Agoston. *Computer Graphics and Geometric Modelling: Implementation & Algorithms*, pages 301–306. Computer Graphics and Geometric Modeling. Springer London, 2005. ISBN 9781846281082.

N. Alsubaie, S. A. Raza, and N. M. Rajpoot. Stain deconvolution of histology images via independent component analysis in the wavelet domain. In *13th IEEE International Symposium on Biomedical Imaging, ISBI*, pages 803–806. IEEE, 2016. doi: 10.1109/ISBI.2016.7493388.

N. Alsubaie, N. Trahearn, S. A. Raza, D. Snead, and N. M. Rajpoot. Stain deconvolution using statistical analysis of multi-resolution stain colour representation. *PLOS ONE*, 12 (1):1–15, 01 2017. doi: 10.1371/journal.pone.0169875.

T. Chen and C. Chefd'hotel. Deep learning based automatic immune cell detection for immunohistochemistry images. In *Machine Learning in Medical Imaging*, 2014.

T. Chen and C. Srinivas. Group sparsity model for stain unmixing in brightfield multiplex immunohistochemistry images. *Computerized Medical Imaging and Graphics*, 46:30 – 39, 2015. ISSN 0895-6111.

A. Dixon, C. Bathany, M. Tsuei, J. White, K. Barald, and S. Takayama. Recent developments in multiplexing techniques for immunohistochemistry. *Expert Rev. Mol. Diagn.*, 15 (9):1171–1186, 2015.

R. Duggal, A. Gupta, R. Gupta, and P. Mallick. SD-layer: Stain deconvolutional layer for cnns in medical microscopic imaging. In *MICCAI*, 2017. ISBN 978-3-319-66179-7.

D. Fassler, S. Abousamra, R. Gupta, C. Chen, M. Zhao, D. Paredes, S. A. Batool, B. Knudsen, L. Escobar-Hoyos, K. Shroyer, D. Samaras, T. Kurç, and J. Saltz. Deep learning-based image analysis methods for brightfield-acquired multiplex immunohistochemistry images. *Diagnostic Pathology*, 15, 2020.

N. Hidalgo-Gavira, J. Mateos, M. Vega, R. Molina, and A. K. Katsaggelos. Blind color deconvolution of histopathological images using a variational bayesian approach. In *IEEE International Conference on Image Processing (ICIP)*, pages 983–987, 2018. doi: 10.1109/ICIP.2018.8451314.

P. Hofman, C. Badoual, F. Henderson, L. Berland, M. Hamila, E. Long-Mira, S. Lassalle, H. Roussel, V. Hofman, E. Tartour, and M. Ilie. Multiplexed Immunohistochemistry for Molecular and Immune Profiling in Lung Cancer-Just About Ready for Prime-Time? *Cancers (Basel)*, 11(3), Feb 2019.

Marius Ilié, Mélanie Beaulande, Saima Ben Hadj, Emmanuel Chamorey, Renaud Schiappa, Elodie Long-Mira, Sandra Lassalle, Catherine Butori, Charlotte Cohen, Sylvie Leroy, et al. Chromogenic multiplex immunohistochemistry reveals modulation of the immune microenvironment associated with survival in elderly patients with lung adenocarcinoma. *Cancers*, 10(9):326, 2018.

Douglas B Johnson, Jennifer Bordeaux, Ju Young Kim, Christine Vaupel, David L Rimm, Thai H Ho, Richard W Joseph, Adil I Daud, Robert M Conry, Elizabeth M Gaughan, et al. Quantitative spatial profiling of pd-1/pd-l1 interaction and hla-dr/ido-1 predicts improved outcomes of anti–pd-1 therapies in metastatic melanomapd-1/pd-l1 interaction and hladr/ido-1 predict anti–pd-1 outcome. *Clinical Cancer Research*, 24(21):5250–5260, 2018.

A. Lahiani, J. Gildenblat, I. Klaman, N. Navab, and E. Klaiman. Generalizing multistain immunohistochemistry tissue segmentation using one-shot color deconvolution deep neural networks. *CoRR*, abs/1805.06958, 2018.

JH Lambert. Photometria sive de mensura et gradibus luminis colorum et umbrae augsburg. *Detleffsen for the widow of Eberhard Klett*, 1760.

M. Macenko, M. Niethammer, J. Marron, D. Borland, J. Woosley, X. Guan, C. Schmitt, and N. Thomas. A method for normalizing histology slides for quantitative analysis. In *ISBI*, 2009. ISBN 978-1-4244-3931-7.

F. Pérez-Bueno, M. López-Pérez, M. Vega, J. Mateos, V. Naranjo, R. Molina, and A. K. Katsaggelos. A tv-based image processing framework for blind color deconvolution and classification of histological images. *Digital Signal Processing: A Review Journal*, 101, June 2020. ISSN 1051-2004. doi: 10.1016/j.dsp.2020.102727.

Romain Remark, Taha Merghoub, Niels Grabe, Geert Litjens, Diane Damotte, Jedd D Wolchok, Miriam Merad, and Sacha Gnjatic. In-depth tissue profiling using multiplexed immunohistochemical consecutive staining on single slide. *Science immunology*, 1(1): aaf6925–aaf6925, 2016.

O. Ronneberger, P. Fischer, and T. Brox. U-net: Convolutional networks for biomedical image segmentation. In *MICCAI*, 2015. ISBN 978-3-319-24574-4.

A. Ruifrok and D. Johnston. Quantification of histochemical staining by color deconvolution. *Anal Quant Cytol Histol.*, 23, 01 2001.

W. C. C. Tan, S. N. Nerurkar, H. Y. Cai, H. H. M. Ng, D.o Wu, Y. T. F. Wee, J. C. T. Lim, J. Yeong, and T. K. H. Lim. Overview of multiplex immunohistochemistry/immunofluorescence techniques in the era of cancer immunotherapy. *Cancer Communications*, 40(4):135–153, 2020. doi: https://doi.org/10.1002/cac2.12023.

D. S. Thommen, V. H. Koelzer, P. Herzig, A. Roller, M. Trefny, S. Dimeloe, A. Kiialainen, J. Hanhart, C. Schill, C. Hess, S. Savic Prince, M. Wiese, D. Lardinois, P. C. Ho, C. Klein, V. Karanikas, K. D. Mertz, T. N. Schumacher, and A. Zippelius. A transcriptionally and functionally distinct PD-1+ CD8+ T cell pool with predictive potential in non-small-cell lung cancer treated with PD-1 blockade. *Nat. Med.*, 24(7):994–1004, 07 2018.

A. Vahadane, T. Peng, A. Sethi, S. Albarqouni, L. Wang, M. Baust, K. Steiger, A. M. Schlitter, I. Esposito, and N. Navab. Structure-preserving color normalization and sparse stain separation for histological images. *IEEE Transactions on Medical Imaging*, 35(8): 1962–1971, Aug 2016. doi: 10.1109/TMI.2016.2529665.

Y. Van Herck, A. Antoranz, M. D. Andhari, G. Milli, O. Bechter, F. De Smet, and F. M. Bosisio. Multiplexed immunohistochemistry and digital pathology as the foundation for next-generation pathology in melanoma: Methodological comparison and future clinical applications. *Frontiers in Oncology*, 11, 2021. ISSN 2234-943X. doi: 10.3389/fonc.2021.636681.

Appendix A. Training and Implementation Details

Training Data. The training set consists of 60 annotated patches from 6 whole slide images. The size of the patches is 1200×1920 at 40x. 40 Patches from 4 cases were used for training and the remaining 20 patches from the other 2 cases were used for validation. For training, the images are resized to 20x and cut up into 400×400 overlapping patches, resulting in a total of 240 labeled training patches.

Models Compared. We train our proposed method *InverseAE* on the 240 patches, without annotation. We compare to the unsupervised approaches:
(1) *LassoReg*: the lasso regression unsupervised method described in (Chen and Chefd'hotel, 2014) which is designed to work on images with 4+ multiplex staining. We used L1 norm weight $\lambda = 10^{-3}$.
(2) *PseudoInv*: an extension of (Ruifrok and Johnston, 2001) for color deconvolution that solves the equation $\boldsymbol{C} = \boldsymbol{S}^{-1} \times \boldsymbol{Y}$ for more than 3 stain vectors using pseudo inverse of $\boldsymbol{S}$.
(3) *Nearest Neighbor* baseline which basically assigns the stain with the closest Euclidean distance to the pixel color value.
Additionally, we use the dot annotations to train with weak supervision:
(4) *ColorAE*: the weakly supervised method in (Abousamra et al., 2020).
(5) *UNet*: a supervised deep learning model based on UNet model architecture (Ronneberger et al., 2015). Different from previous methods, UNet's output is not stain concentration maps but rather likelihood maps. For each pixel, the output is the probability that the pixel belongs to each stain class. Superpixel annotation maps (Achanta et al., 2012) derived from the dot labels are used as the ground truth labels.

F-score Computation. We computed the F-score for each biomarker/cell type, as follows: a true positive is a predicted stain segment that intersects with an annotation dot, a false positive is a segment that doesn't intersect with any annotation dot, a false negative is an annotation dot that does not intersect with any predicted segment.

Appendix B. Ablation Study.

Here we present ablation studies on the design choices for our unsupervised model *InverseAE*. In Table 3 we present the F-score results on the 96 annotated patches using variations from our proposed method. First, the results show the importance of the inverse reconstruction loss. Without it (rows 1 and 2), the predicted maps are not representative of the stains visually present in the mIHC image. This is clear from the very low F-scores. Second, replacing the inverse reconstruction loss with a L1 sparsity constraint (row 2) is not sufficient to get representative concentration maps. We notice sparsity in the prediction nevertheless the prediction is not correlated with the observed stains. The dominating stains in the prediction are mostly CD3's yellow and CD8's purple, while the tumor (brown) and the CD16 (black) biomarkers are missing, as evidenced by their zero F-score in the table. Third, without the conditional autoencoder (row 3) i.e., predicting all the stains at once without target stains conditional input, the scores are lower and the model does not generalize well. The conditional input prevents the model from overfitting and allows the model to better capture the target stains in the image.

Table 3: Ablation study on unsupervised model design InverseAE, evaluated with F-score of stain segmentations with respect to dot annotations on 96 patches from 42 cases.

Inverse Reg.	Conditional AE	$L1$ Sparsity	CD3	CD4	CD8	CD16	CD20	Tumor	Mean
	✓		0.235	0.307	0.409	0.121	0.326	0.147	0.257
	✓	✓	0.215	0.228	0.337	0.000	0.300	0.000	0.180
✓			0.482	0.501	0.753	0.324	0.274	0.220	0.426
✓	✓		**0.644**	**0.530**	**0.813**	**0.632**	**0.327**	**0.556**	**0.584**

Appendix C. RGB to HSL Conversion.

We include here the formulas for obtaining saturation and lightness from RGB for their relevance. The complete conversion algorithm including hue can be found in (Agoston, 2005). To convert from a normalized RGB color (r, g, b) to HSL space, we first define the variables M and m that represent the maximum and minimum of (r, g, b), respectively :

$$M = max(r, g, b) \tag{13}$$

$$m = min(r, g, b) \tag{14}$$

The formula for lightness L:

$$L = \frac{1}{2}(M + m) \tag{15}$$

The formula for saturation S:

$$S = \begin{cases} 0 & \text{if } L = 0 \; or \; L = 1. \\ \frac{M-m}{1-|2L-1|} & \text{otherwise.} \end{cases} \tag{16}$$

For the inverted color $(r', g', b') = (1 - r, 1 - g, 1 - b)$, the formulas become:

$$M' = 1 - m \tag{17}$$

$$m' = 1 - M \tag{18}$$

$$L' = 1 - L \tag{19}$$

$$S' = \begin{cases} 0 & \text{if } L' = 0 \; or \; L' = 1. \\ \frac{M'-m'}{1-|2L'-1|} & \text{otherwise.} \end{cases} = \begin{cases} 0 & \text{if } L = 0 \; or \; L = 1. \\ \frac{M-m}{1-|2L-1|} & \text{otherwise.} \end{cases} = S \tag{20}$$